Capillary deformation of ultrathin glassy polymer films by air nanobubbles

Shuai Ren [1,*] Christian Pedersen,[2,*] Andreas Carlson [2] Thomas Salez [3,4,†] and Yuliang Wang [1,5,‡]

[1]*School of Mechanical Engineering and Automation, Beihang University, 37 Xueyuan Road, Haidian District, Beijing 100191, China*

[2]*Mechanics Division, Department of Mathematics, University of Oslo, 0316 Oslo, Norway*

[3]*Univ. Bordeaux, CNRS, LOMA, UMR 5798, F-33405 Talence, France*

[4]*Global Station for Soft Matter, Global Institution for Collaborative Research and Education, Hokkaido University, Sapporo, Hokkaido 060-0808, Japan*

[5]*Beijing Advanced Innovation Center for Biomedical Engineering, Beihang University, 37 Xueyuan Road, Haidian District, Beijing 100191, China*

(Received 5 March 2020; accepted 14 September 2020; published 30 October 2020)

Confined glasses and their anomalous interfacial rheology raise important questions in fundamental research and numerous practical applications. In this work, we study the influence of interfacial air nanobubbles on the free surface of ultrathin high-molecular-weight glassy polystyrene films immersed in water, in ambient conditions. In particular, we reveal the counterintuitive fact that a soft nanobubble is able to deform the surface of a rigid glass, forming a nanocrater with a depth that increases with time. By combining *in situ* atomic-force-microscopy measurements and a modified lubrication model for the liquidlike layer at the free surface of the glass, we demonstrate that the capillary pressure in the nanobubble together with the liquidlike layer at the free surface of the glass determine the spatiotemporal growth of the nanocraters. Finally, from the excellent agreement between the experimental profiles and the numerical solutions of the governing glassy thin-film equation, we are able to precisely extract the surface mobility of the glass. In addition to revealing and quantifying how surface nanobubbles deform immersed glasses, until the latter eventually dewet from their substrates, our work provides a novel, precise, and simple measurement of the surface nanorheology of glasses.

DOI: 10.1103/PhysRevResearch.2.043166

I. INTRODUCTION

The glass transition has been a major enigma in solid-state physics [1] for almost a century, leading to an important literature for the bulk case [2]. Besides a hypothetical underlying phase transition, the tremendous dynamical slowing down of glass-forming supercooled liquids has been attributed to molecular caging, and the associated requirement for cooperative relaxation [3] in a region of a certain cooperative size [4].

The quest for the latter observable, and its possible divergence, led to an alternative strategy: the study of glasses in confinement [5–7]. In the particular case of thin polymer films, anomalies have been reported, such as reductions of the apparent glass-transition temperature T_g at small film thicknesses [8,9], where the presence of free surfaces played an important role [10]. Furthermore, space-dependent T_g values were inferred from local measurements [11]. Besides, the free surface of a polymer glass was discovered to be much more mobile than the bulk, which was attributed to the existence of a nanometric liquidlike superficial layer capable to flow under external constraints [12–17], or equivalently for small enough molecules to undergo surface diffusion [18–20] as in crystals [21], which could even lead to striking engulfment phenomena [22]. The previous Stokes-Einstein-like equivalence between surface flow and surface diffusion in the mobile layer was shown to be eventually broken for long-enough surface polymer chains due to their anchoring into the bulk matrix [23], and ultimately the commensurability of their typical size with the sample thickness itself [24,25]. Finally, among other interesting properties, spatial heterogeneities were associated with the dynamics of thin glassy polymer films [26]. To rationalize these observations, various numerical approaches [27,28] and theoretical models [29–34] have been proposed, but a unifying picture is still at large.

In this work, we study the influence of air nanobubbles spontaneously created at the free surface of ultrathin high-molecular-weight glassy polystyrene (PS) films when immersed in water, and in ambient conditions [35,36]. In contrast to the bubble-inflation technique used for freestanding viscoelastic membranes [37], there is here no need for an externally driven inflation, and the glassy films are supported onto rigid silicon wafers and thus much less compliant. The nanobubbles are gaseous air domains with nanometric height and width. As a consequence of these small sizes, and from the Young-Laplace equation, the pressure inside the bubble

*These authors contributed equally to this work.
†thomas.salez@u-bordeaux.fr
‡wangyuliang@buaa.edu.cn

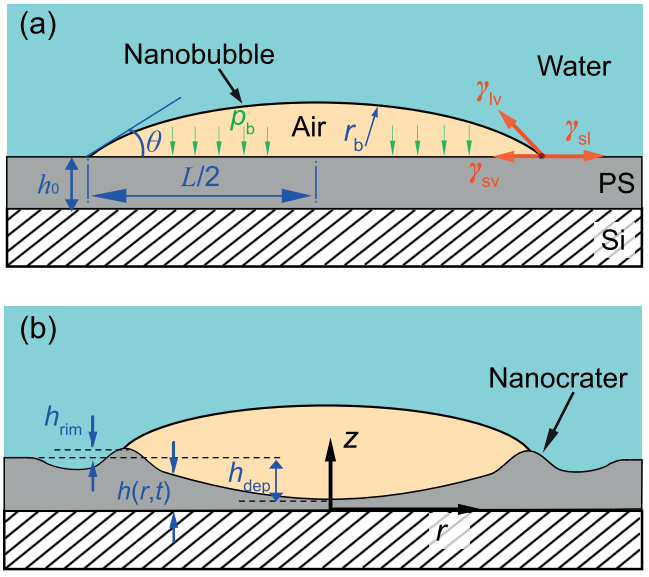

FIG. 1. Schematic of the bubble-PS film interaction. (a) An air nanobubble spontaneously forms at the PS-water interface right after immersion of the glassy PS sample in water. (b) Subsequently, a nanocrater appears beneath the nanobubble, and grows with time, as the liquidlike layers at both PS-fluid interfaces flow due to the capillary pressure gradient.

can reach up to ∼10 bar, which—despite being much smaller than the yield stress of the bulk glass—can lead to an external driving force for the flow of the liquidlike layer at the free surface of the glass. Consequently, a nanoscopic crater is formed underneath the bubble, and grows in size with time, as observed using an atomic-force microscope (AFM). The latter observations are discussed in the context of a modified lubrication model for the capillary-driven flow of the liquidlike layer at the free surface of the glassy film, under an external driving force. The excellent agreement between the experimental AFM profiles and the numerical solutions of the axisymmetric glassy thin-film equation yields a novel, precise, and simple measurement of the surface mobility of glasses. The value found for the latter is compared to values in the literature, and discussed in terms of polymer entanglements and anchoring effects in confinement. Finally, the model predicts a dewetting scenario for ultrathin polymer films, which might have important practical consequences.

II. EXPERIMENTAL SETUP

A schematic representation of the bubble-PS film interaction is shown in Fig. 1, where we define the bubble's contact diameter L, the bubble's radius of curvature r_b, the equilibrium contact angle θ, and the initial PS film thickness h_0. Note that L, r_b, and θ are related through volume conservation. According to the Young-Laplace equation, the pressure inside the bubble reads $p_b = p_{am} + 2\gamma_{lv}/r_b$, where γ_{lv} is the water-air surface tension and p_{am} is the ambient water pressure. In the following, we will quantify how the capillary pressure gradient can lead to the deformation of the glassy PS film and to the spatiotemporal evolution of the PS nanocrater. The latter is characterized by its depth h_{dep} and rim height h_{rim}.

Ultrathin PS films with three different thicknesses $h_0 \in \{2.8 \pm 0.6, 4.9 \pm 0.6, 7.1 \pm 0.8\}$ nm were prepared by spincoating a solution of PS (Sigma-Aldrich) in toluene onto a silicon wafer, at different toluene mass fractions $\{0.07, 0.10, 0.08\}$ wt% and rotational speeds of $\{1200, 1200, 1000\}$ rpm, respectively. The thicknesses of the PS films were measured by a scratching method [38]. The molecular weight of PS is about 350 kg/mol. After spincoating, the PS films were baked inside an oven at a temperature of 45°C for 4 h, to evaporate the remaining toluene. Here, we applied the temperature-exchange method to generate nanobubbles: cold deionized (DI) water at about 4°C was deposited on the PS films at about 30°C by a glass syringe. Upon immersion, nanobubbles were spontaneously nucleated.

An AFM (Resolve, Bruker, USA) in tapping mode was used to image the samples both in air and water. A silicon NSC36/Al BS cantilever (MikroMasch) with a tip radius <8 nm and a quoted stiffness of 1.0 N/m was used. The measured resonance frequencies of the cantilever in air and water were about 76 and 23 kHz, respectively. To minimize the force applied on the nanobubbles and sample surfaces, the setpoint for imaging was set to be only 95%–97% of the free amplitude. While imaging in air and water, the resonance frequencies were selected as the driving ones. The samples were scanned at a rate of 1.5 Hz with a scan angle of 0°.

III. RESULTS AND DISCUSSION

Figure 2(a) shows a typical AFM image of the PS film in air with a thickness $h_0 = 4.9 \pm 0.6$ nm. The root-mean-squared roughness is about 0.22 nm. After immersion in deionized (DI) water at room temperature, nanobubbles with diameters ranging from 30 to 100 nm spontaneously nucleated [Fig. 2(b)] at the PS-water interface [39]. The PS sample was kept in water for $t_b \approx 240$ min, before the water was removed and the sample surface was dried in air for $t - t_b \approx 250$ min. The same area of the sample was then scanned again with the AFM, as shown in Fig. 2(c). One observes the existence of nanocraters into the PS film. These nanocraters were generated at the exact same locations where the nanobubbles resided, when the sample was immersed in water (see also Fig. 4 in Appendix A for details).

The cross-sectional profiles for five different nanobubbles and their associated nanocraters (sorted by increasing nanobubble size) are shown in Figs. 2(d)–2(h). Interestingly, these profiles qualitatively ressemble the ones obtained on low-molecular-weight PS after embedding and subsequent removal of gold nanoparticles [12]. Moreover, it is clear that the lateral sizes of the nanocraters are approximately equal to the sizes of the nanobubbles—a commensurability valid for all samples in this study (see Fig. 5 in Appendix B). Nanobubbles with contact diameters $L \leqslant 50$ nm typically generate steeper nanocraters, and h_{dep} increases with L for those [Figs. 2(d)–2(f)]. When the contact diameter L is larger than 50 nm, the nanocraters are not as curved. Larger bubbles generate shallower craters with decreased h_{dep} and h_{rim} [Figs. 2(g) and 2(h)]. With further increased L, nanocraters with nearly flat bottoms are even created (see also Fig. 4 in Appendix A for details).

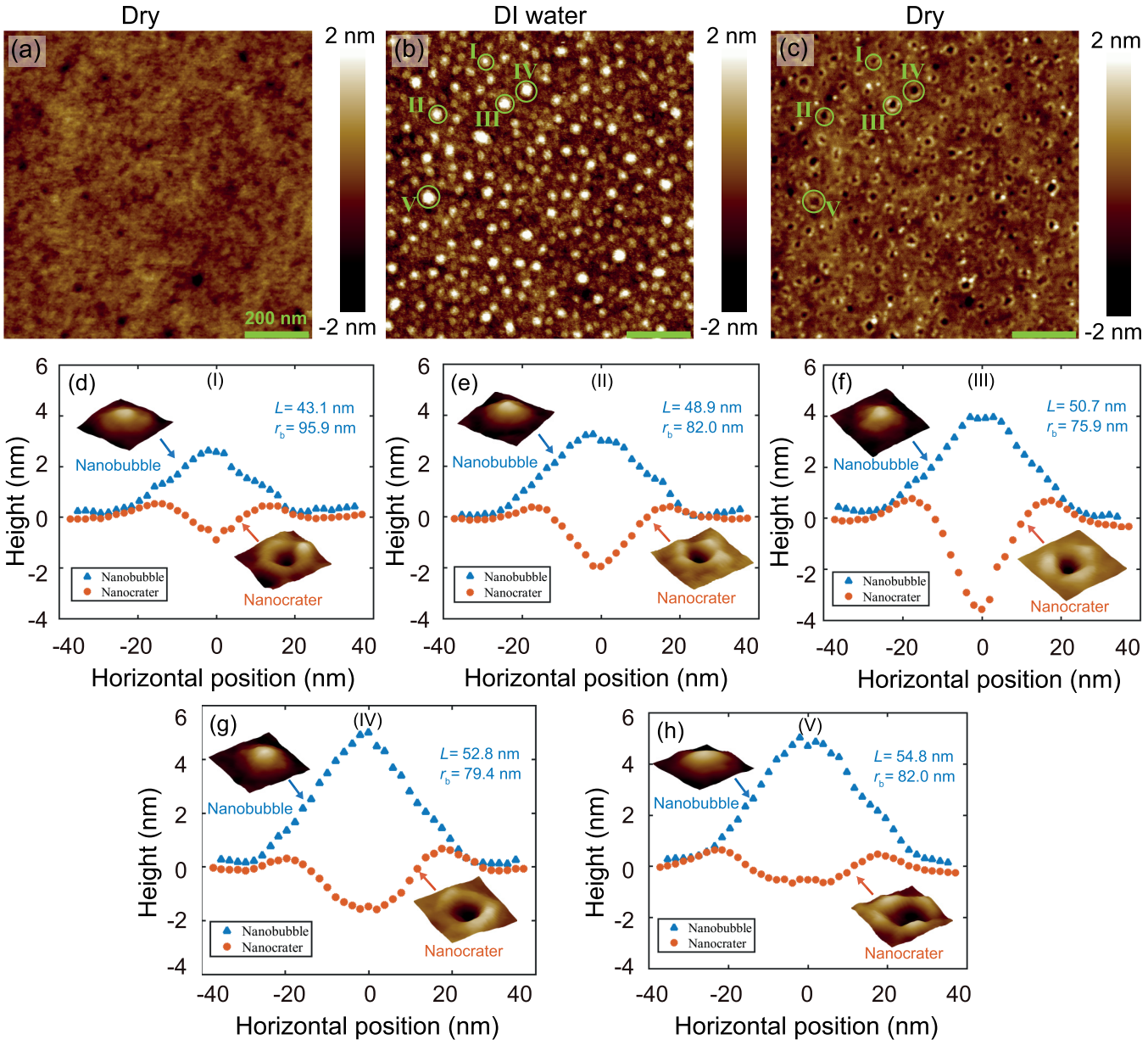

FIG. 2. Typical AFM images of an ultrathin glassy PS film with thickness $h_0 = 4.9 \pm 0.6$ nm in various situations: (a) before immersion in water; (b) after immersion in water, where nanobubbles (white) with an average contact diameter of 50 nm appear on top of it; (c) after immersion in water for $t_b \approx 240$ min, and subsequent removal of water followed by drying in air during $t - t_b \approx 250$ min. (d–h) Five cross-sectional profiles of nanobubble-nanocrater couples (sorted by increasing L values): $L = 43.1$ nm and $r_b = 95.9$ nm (d, couple I); $L = 48.9$ nm and $r_b = 82.0$ nm (e, couple II); $L = 50.7$ nm and $r_b = 75.9$ nm (f, couple III); $L = 52.8$ nm and $r_b = 79.4$ nm (g, couple IV); $L = 54.8$ nm and $r_b = 82.0$ nm) (h, couple V). The insets in each of those five panels are the 3D AFM images of the nanobubbles and the corresponding nanocraters.

To rationalize these observations, we invoke a theoretical model that combines two ingredients: (i) the existence of a liquidlike layer with viscosity η and thickness h_m of a few nanometers at the free surface (i.e., exposed to any fluid) of the glassy PS film [12,14]; and (ii) a lubrication flow in this liquidlike layer [15], driven by the pressure jump between p_b and p_{am} at the contact line where the three phases intersect, and opposed by the restoring capillary force due to the induced curvature at the PS-fluid interfaces. We note that the PS films employed in this work have thicknesses of a few nanometers only, which are: (i) comparable to the typical thickness of the liquidlike layer [7]; and (ii) much smaller than the radius of gyration of 350 kg/mol PS (tens of nanometers). Therefore, the PS chains are mostly located in the liquidlike layer, they are expected to exhibit a reduced entanglement density compared to the one in thicker films [40–43], and we expect no major anchoring effect [23]. Since the liquidlike layer thickness h_m is much smaller than the typical horizontal size L, the viscous flow in the layer can be described by lubrication theory [44], where the velocity is predominantly in the radial direction, the pressure is constant across the thickness of the liquidlike layer [45–47], and the viscous forces therein are

balanced by the tangential pressure gradient discussed above. As the stresses remain relatively low compared to usual yield stresses and piezoviscous thresholds for polymers glasses and melts, the viscosity η is assumed to be a constant.

In general, the stress and deformation fields associated to one bubble could be affected by the neighboring bubbles. In a recent study involving two microsized droplets on a polymer film [48] (see also Fig. 6 in Appendix C), it is indeed found that the effective interaction between the two microdroplets is strongly influenced by their distance d, contact diameter L, and the film thickness h_0. When $d > L/2$ or $d \gg h_0$, the two-body interaction mediated by the film vanishes. In the present work, the average value of d is around 50 nm, L is in between 20 nm and 45 nm, and h_0 is less than 8 nm. It is thus clear that d is much bigger than $L/2$ and h_0. Therefore, we neglect the influence of neighboring bubbles in the model.

We define $h(r,t)$ as the total thickness profile of the PS film (see Fig. 1), assumed to be axisymmetric given the symmetry of the nanobubble, where r is the horizontal radial spatial coordinate, and t is time. We further assume small slopes for the PS-fluid interfaces, as well as a no-slip boundary condition at the bottom of the mobile layer, located at $z = h(r,t) - h_m$, and a no-shear boundary condition at the PS-fluid interfaces, located at $z = h(r,t)$. All together, this leads to the axisymmetric version of the glassy thin-film equation [15], with a novel source term due to the presence of the nanobubble:

$$\frac{\partial h(r,t)}{\partial t} + \frac{h_m^3}{3\eta r}\frac{\partial}{\partial r}\left\{r\frac{\partial}{\partial r}\left[\frac{\gamma_i(r)}{r}\frac{\partial}{\partial r}\left(r\frac{\partial}{\partial r}h(r,t)\right) - p_i(r)\right]\right\} = 0, \tag{1}$$

where the surface energy $\gamma_i(r)$ indicates γ_{SL} (PS-water) for $r \geqslant L/2$ and $t < t_b$, as well as γ_{SV} for either $t > t_b$, or $t < t_b$ and $r < L/2$; while the external pressure $p_i(r)$ indicates p_b for $r \leqslant L/2$ and $t < t_b$, as well as p_{am} for either $t > t_b$, or $t < t_b$ and $r > L/2$. Due to the constant liquidlike layer thickness h_m, the equation is linear, and formally resembles the capillary-driven thin-film equation for bulk flow under perturbative profile variations [46,49]. Just before the formation of the nanobubble (assumed to be instantaneous), the PS film has a uniform thickness $h(r, t = 0) = h_0$, which we use as an initial condition.

We now nondimensionalize Eq. (1) by rescaling the variables through $h = H\,h_0$, $r = R\,L/2$, $t = T\,3\eta L^4/(16\gamma_{SV}h_m^3)$, and $t_b = T_b\,3\eta L^4/(16\gamma_{SV}h_m^3)$, which leads to the dimensionless form of Eq. (1):

$$\frac{\partial H(R,T)}{\partial T} + \frac{1}{R}\frac{\partial}{\partial R}\left\{R\frac{\partial}{\partial R}\left[\frac{1-\alpha(T)\Theta(R-1)}{R}\frac{\partial}{\partial R}\left(R\frac{\partial}{\partial R}H(R,T)\right) - \beta(T)\Theta(1-R)\right]\right\} = 0, \tag{2}$$

where Θ is the Heaviside function, $\alpha(T) = (\gamma_{SV} - \gamma_{SL})\Theta(T_b - T)/\gamma_{SV}$ and $\beta(T) = L^2\gamma_{LV}\Theta(T_b - T)/(2h_0 r_b \gamma_{SV})$. We solve Eq. (2) numerically from the initial condition $H(R, T = 0) = 1$, by using a finite-element method where the equation is divided into two coupled second-order partial differential equations involving two fields [50]: the height $H(R,T)$ and the total pressure $P(R,T) = \frac{\alpha(T)\Theta(R-1)-1}{R}\frac{\partial}{\partial R}[R\frac{\partial}{\partial R}H(R,T)] + \beta(T)\Theta(1-R)$. The fields are discretized with linear elements, and the coupled equations are solved with a Newton solver from the FEniCS library [51]. The numerical routine is performed with a constant time step $\Delta T = 5 \times 10^{-4}$ and a uniform spatial discretization step $\Delta R = 5 \times 10^{-4}$. Finally, as spatial boundary conditions at $R = 0$, we set the first-order derivatives of the two fields to be zero due to symmetry. Besides, we choose the size of the numerical domain such that no dynamics occurs at the large-R boundary, and we thus impose the first-order derivatives to be equal to zero too at this boundary.

Figure 3(a) shows an example of a numerical solution of Eq. (2). It includes two subsequent steps. The first one (corresponding to the dimensionless T from 0 to 0.04) is the nanocrater growth process with a nanobubble on top of the nanocrater. During the process, both the dimensionless depth h_{dep}/h_0 of the nanocrater and the dimensionless height h_{rim}/h_0 of the rim increase monotonically with dimensionless time. The second step (corresponding to the dimensionless T from 0.04 to 0.128) is the partial recovery of the nanocrater after the nanobubble is removed. The depth and height decrease monotonically with time. As the fluid in the liquidlike layer gets displaced, we also observe a continuous lateral shift in the dimensionless horizontal position of the rim.

In Figs. 3(b)–3(f), we fit the numerical solutions to the experimental profiles, for five nanocraters created by the five selected nanobubbles [shown in Figs. 2(d)–2(h)] of increasing contact diameters L from b to f. To do so, we first put back dimensions in the numerical solutions, by using the experimental parameters: $t - t_b = 250$ min, $\gamma_{SV} = 40.7$ mN/m, $\gamma_{LV} = 72.8$ mN/m, and $h_0 = 4.9 \pm 0.6$ nm, as well as the values of t_b, L and r_b for each nanobubble. As we determine the geometric parameters from a single snapshot of the nanobubble profile, which is not perfectly symmetric, there is some uncertainty in the obtained values. To account for this uncertainty, we multiply L and r_b by a dimensionless free parameter ρ. For all experiments in this study, the value of the latter is found to be in the 0.3–0.5 range, which is reasonably close to 1 and thus acceptable. We observe that the numerical solutions show a good agreement with experimental cross-sectional profiles for all five exemplary nanocraters. The depth h_{dep} of the nanocraters first increases and then decreases with increasing L. Interestingly, we find that it is actually r_b that determines h_{dep}. With increasing L, r_b first decreases from 95.9 nm (bubble I) to 75.9 nm (bubble III). Then it increases from 75.9 nm (bubble III) to 82.0 nm (bubble V). The smaller r_b leads to the larger deformation in the PS film, i.e., the larger magnitudes of the rim height h_{rim} and crater depth h_{dep}. This is expected due to the Laplace pressure of the nanobubbles, that scales as $\sim 1/r_b$, and that drives the deformation of the PS layer.

From the fitting procedure detailed above, we extract a single relevant free parameter: the surface mobility $h_m^3/(3\eta) =$

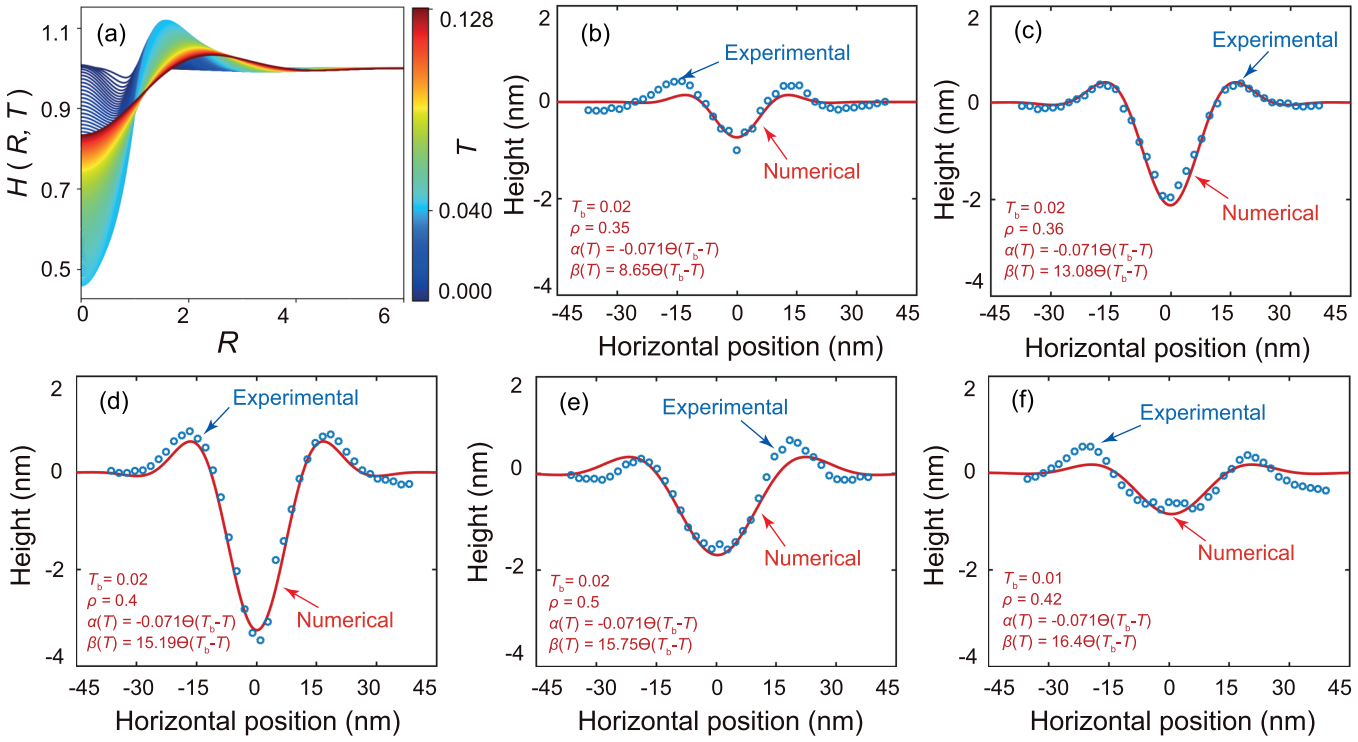

FIG. 3. Deformation of the PS film: (a) Numerical solution of Eq. (2) over a time interval $T \in [0, 0.128]$, for $T_b = 0.01$, $\alpha(T) = -0.071\,\Theta(T_b - T)$, and $\beta(T) = 5\,\Theta(T_b - T)$. (b–f) Cross-sectional AFM profiles (blue circular markers) in air for the five selected nanocraters in Figs. 2(d)–2(h), and corresponding best fit (red solid curves) to the numerical solution with $T_b = 0.02$, $\rho = 0.35$, $\alpha(T) = -0.071\,\Theta(T_b - T)$, and $\beta(T) = 8.65\,\Theta(T_b - T)$ (b); $T_b = 0.02$, $\rho = 0.36$, $\alpha(T) = -0.071\,\Theta(T_b - T)$, and $\beta(T) = 13.08\,\Theta(T_b - T)$ (c); $T_b = 0.02$, $\rho = 0.4$, $\alpha(T) = -0.071\,\Theta(T_b - T)$, and $\beta(T) = 15.19\,\Theta(T_b - T)$ (d); $T_b = 0.02$, $\rho = 0.5$, $\alpha(T) = -0.071\,\Theta(T_b - T)$, and $\beta(T) = 15.75\,\Theta(T_b - T)$ (e); $T_b = 0.01$, $\rho = 0.42$, $\alpha(T) = -0.071\,\Theta(T_b - T)$, and $\beta(T) = 16.4\,\Theta(T_b - T)$ (f). Note that the horizontal and vertical origins are arbitrarily shifted.

$2.31^{+1.73}_{-1.92} \times 10^{-10}$ nm^3/(Pa.s) of 350 kg/mol PS at room temperature. Regardless of the total PS film thickness, and the nanobubble geometry, the different experiments self-consistently exhibit the same value of surface mobility. Previously, the surface mobility of glassy PS was investigated around T_g for a range of molecular weights [14,15,52]. Interestingly, the extrapolation to room temperature of the Arrhenius-like trends in these works would lead to a surface mobility over one order of magnitude lower than the one reported here. This brings two possible nonexclusive scenarios: (i) a saturation of the surface mobility at low temperature; (ii) a reduction of the entanglement density, and thus viscosity, in strong confinement. Indeed, while it is known that in the near-T_g region the surface mobility exhibits an Arrhenius-like dependence in the temperature, which is characteristic of a liquidlike behavior [15,52], the mobility saturates at lower temperatures [12]. Regarding the entanglement density, it is found that polymer molecules at interfaces are less entangled than their bulk counterparts [41–43]. The entanglement density collapses rapidly when the film thickness becomes lower than the end-to-end distance of the polymer chains [40,53]. This further implies a reduction in viscosity [54–56]. For these reasons, since the PS films used here are colder and thinner than that in studies from the literature, one could expect a much higher mobility compared to Arrhenius-like extrapolations of the literature results.

Finally, we stress that the PS deformation profiles are transient, and that they in fact will continue to evolve with increasing time [see Fig. 3(a)], although very slowly. Moreover, a careful mathematical analysis of Eq. (1) reveals the absence of any relevant stationary state, which implies a dramatic consequence: due to the existence of a liquidlike surface layer, and provided the films are thin enough (i.e., h_0 close to h_m) to avoid anchoring effects at large molecular weights [23], the presence of surface nanobubbles should eventually lead to the dewetting of any ultrathin glassy PS film [57,58]. The critical time for dewetting is solely controlled by the parameters θ, γ_{SV}, γ_{LV}, h_0, and L (or r_b, due to volume conservation) above, as well as the surface mobility $h_m^3/(3\eta)$.

IV. CONCLUSION

As a conclusion, we have shown that immersing ultrathin glassy polystyrene films in water, in ambient conditions, leads to the spontaneous nucleation of air nanobubbles, which then generate nanocraters into the free surface of the PS films. The mechanism of such a dynamical deformation process is found by combining experimental atomic-force microscopy with a mathematical model based on lubrication theory applied to the liquidlike layer present at the free surface of a glassy film. The liquidlike layer is driven to flow by the pressure jump at the contact line where the three phases intersect, between the

nanobubble's inner Laplace pressure and the outer ambient pressure, and opposed by the capillary force due to the induced curvature at the PS-fluid interfaces. Since the Laplace pressure scales as the inverse of the bubble's radius of curvature, the size of the nanocraters can be finely controlled. From the excellent agreement between the experimental profiles and the numerical solutions of the modified glassy thin-film equation, we extract the surface mobility of the glassy films. Comparison of the surface mobility with extrapolated results from the literature points towards the possible saturation of surface mobility at low temperature, and/or the reduction of polymeric entanglement density (and thus viscosity) in confinement. All together, our work provides a novel, precise, and simple measurement of the surface nanorheology of glasses. Furthermore, our results highlight the influence of surface nanobubbles on the stability of immersed ultrathin glassy polymer films: the nanobubbles can drive the film towards dewetting, which would have important consequences for nanoimprint lithography [59] and nanomechanical data storage [60], to name a few.

ACKNOWLEDGMENTS

The authors thank James Forrest, Robert Style, Detlef Lohse, and Jacco Snoeijer for interesting discussions. Y.W. and S.R. appreciate financial support from the National Natural Science Foundation of China (Grants No. 51775028 and No. 52075029) and the Beijing Natural Science Foundation (Grant No. 3182022). A.C. is grateful for the financial support from the Norwegian Research Council, Projects No. 263056 and No. 301138.

APPENDIX A: NANOBUBBLE-NANOCRATER CORRELATION

Figure 4(a) shows AFM image of nanobubbles on the surface of an ultrathin PS glassy film in DI water. After water was removed, the AFM image of the exact same scanning area is shown in Fig. 4(d). From the figure, one can see that the sample surface is covered with nanocraters. To demonstrate that those nanocraters were indeed produced at the exact same locations as the nanobubbles, the AFM images of nanobubbles and nanocraters were segmented, as shown in Figs. 4(b) and 4(e), respectively. The obtained binary images of nanobubbles and nanocraters are shown in Figs. 4(c) and 4(f). The overlapped image [Fig. 4(g)] from the two binary images indicates that the nanocraters were generated at the exact same locations as the nanobubbles.

APPENDIX B: NANOCRATER FORMATION ON SAMPLES WITH DIFFERENT THICKNESSES

Three PS films of different thicknesses were used. Figures 5(a), 5(d) and 5(g) are AFM images in air of the three PS films with thicknesses of 2.8 $\pm$ 0.6 nm, 4.9 $\pm$ 0.6 nm, and 7.1 $\pm$ 0.8 nm, respectively. After immersion in DI water, the obtained AFM images are shown in Figs. 5(b), 5(e) and 5(h). One can see that nanobubbles with different sizes were produced on the surface of the PS samples. After DI water was removed [Figs. 5(c), 5(f) and 5(i)], nanocraters were observed on the surface of the PS samples. The sizes of the nanocraters are highly correlated with those of the nanobubbles. Larger nanobubbles lead to nanocraters with larger lateral widths.

For the sample with a thickness of 2.8 nm, one could observe pre-existed holes. However, we believe that these holes

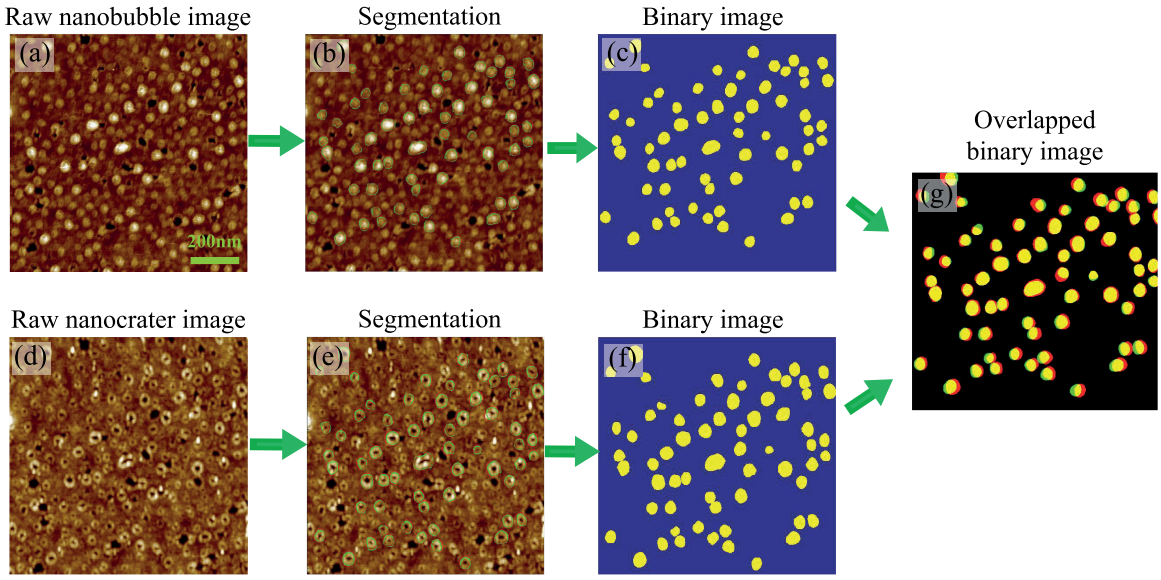

FIG. 4. (a) Raw AFM image of nanobubbles at the surface of an ultrathin glassy PS film in deionized (DI) water. (b) Segmentation of the nanobubble image. The green contours are extracted nanobubble boundaries. (c) The resulting binary image. The yellow masks are extracted nanobubble areas. (d) Raw AFM image of nanocraters at the exact same scanning area as in panel (a). (e) Segmented nanocrater image. (f) Resulting binary image of the segmented nanocrater image. The yellow masks are extracted nanocrater areas. (g) Superposition of the two binary images.

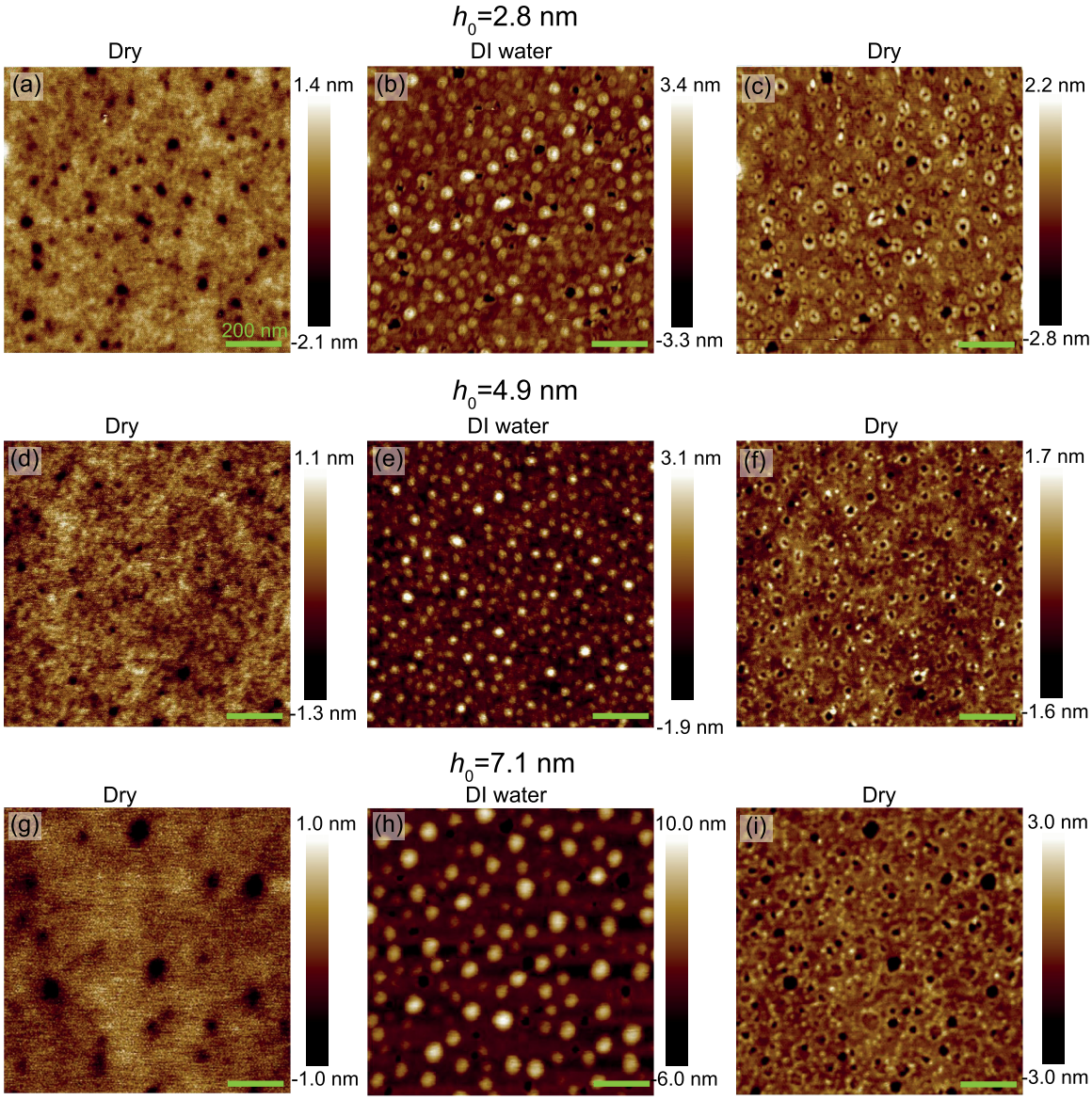

FIG. 5. (a) AFM image of the PS film with a thickness of 2.8 nm, obtained in air. (b) AFM image of the nanobubbles nucleated in the same scanning area as in panel (a), after immersion in DI water. (c) AFM image of the nanobubble-induced nanocraters, after DI water was removed. (d) AFM image of the PS film with a thickness of 4.9 nm, obtained in air. (e) AFM image of the nanobubbles nucleated in the same scanning area as in (d), after immersion in DI water. (f) AFM image of the nanobubble-induced nanocraters, after DI water was removed. (g) AFM image of the PS film with a thickness of 7.1 nm, obtained in air. (h) AFM image of the nanobubbles nucleated in the same scanning area as in panel (g), after immersion in DI water. (i) AFM image of the nanobubble-induced nanocraters, after DI water was removed.

are not due to the dewetting of the sample at room temperature (which would then impact the nanocrater dynamics), based on the following fact. If the film was close to dewetting, one would expect more holes to appear and grow with time. Figure 5 clearly shows that the number, locations, as well as sizes of the pre-existed holes do not change before and after water immersion. This clearly indicates that the surface of the solid-liquid interface is stable during the experiment, besides the nanocrater dynamics at stake. It is highly possible that the pre-existed holes were generated during the sample-preparation process, through the thermal-annealing step in particular.

APPENDIX C: INFLUENCE OF NEIGHBORING NANOBUBBLES

For a given nanocrater, it is *a priori* possible that the stress and deformation fields are influenced by neighboring nanobubbles. The influence from neighboring nanobubbles depends on the following geometrical parameters: the distance d between the bubbles, the contact radius $R_c = L/2$, and the substrate's thickness h_0. When $d \gg R_c$ or $d \gg h_0$, we expect the effects from neighboring bubbles to vanish, which was verified in microdroplet experiments [48] (see also Fig. 6). According to the latter, when d/R_c becomes comparable to

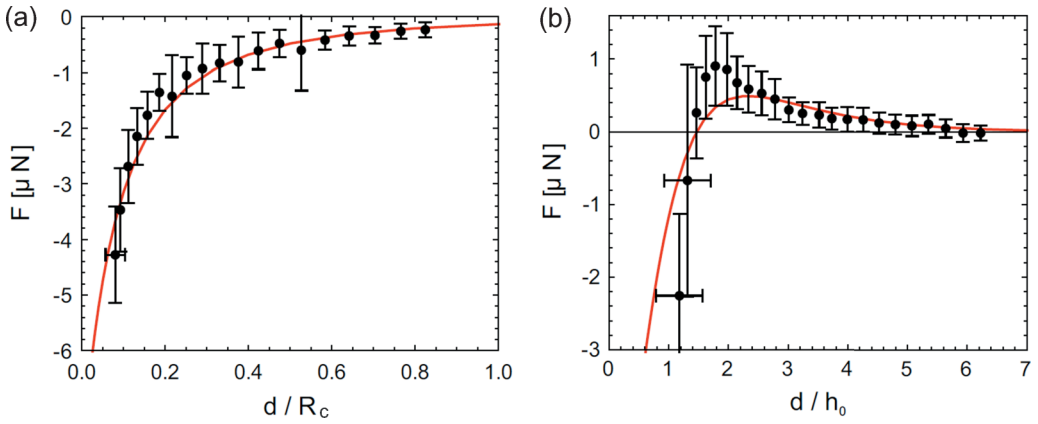

FIG. 6. Reproduction of Fig. 2 from Ref. [48]. (a) Interaction force (dots: measurements; line: model) F between two neighboring droplets as a function of the ratio between their separation distance d and the contact radius R_c. (b) Interaction force (dots: measurements; line: model) F between two neighboring droplets as a function of the ratio between their separation distance d and the substrate's thickness h_0.

or less than 1, and for large enough h_0, there is an attractive force F between the two droplets [see Fig. 6(a)]. Besides, when d/h_0 gets sufficiently larger than 1, the force becomes repulsive [see Fig. 6(b)].

In the present work, the distance d between two neighboring nanobubbles is around 50 nm. The contact radii of the nanobubbles are in between 20 nm and 45 nm. The initial thicknesses of the three different ultrathin PS films are $h_0 = 2.8 \pm 0.6$, 4.9 ± 0.6, and 7.1 ± 0.8 nm. Therefore, $d/R_c > 1$ and $d/h_0 \gg 1$, such that the influence of neighboring nanobubbles can be safely neglected in our study (see Fig. 6).

[1] P. W. Anderson, Science **267**, 1615 (1995).
[2] L. Berthier and G. Biroli, Rev. Mod. Phys. **83**, 587 (2011).
[3] G. Adam and J. H. Gibbs, J. Chem. Phys. **43**, 139 (1965).
[4] E. Donth, J. Polym. Sci., Part B: Polym. Phys. **34**, 2881 (1996).
[5] C. L. Jackson and G. B. McKenna, J. Chem. Phys. **93**, 9002 (1990).
[6] J. A. Forrest and K. Dalnoki-Veress, Adv. Colloid Interface Sci. **94**, 167 (2001).
[7] M. D. Ediger and J. A. Forrest, Macromolecules **47**, 471 (2014).
[8] J. L. Keddie, R. A. L. Jones, and R. A. Cory, Europhys. Lett. **27**, 59 (1994).
[9] J. A. Forrest, K. Dalnoki-Veress, J. R. Stevens, and J. R. Dutcher, Phys. Rev. Lett. **77**, 2002 (1996).
[10] O. Bäumchen, J. D. McGraw, J. A. Forrest, and K. Dalnoki-Veress, Phys. Rev. Lett. **109**, 055701 (2012).
[11] C. J. Ellison and J. M. Torkelson, Nat. Mater. **2**, 695 (2003).
[12] Z. Fakhraai and J. A. Forrest, Science **319**, 600 (2008).
[13] M. Ilton, D. Qi, and J. A. Forrest, Macromolecules **42**, 6851 (2009).
[14] Z. Yang, Y. Fujii, F. K. Lee, C.-H. Lam, and O. K. C. Tsui, Science **328**, 1676 (2010).
[15] Y. Chai, T. Salez, J. D. McGraw, M. Benzaquen, K. Dalnoki-Veress, E. Raphael, and J. A. Forrest, Science **343**, 994 (2014).
[16] H. Kim, Y. Cang, E. Kang, B. Graczykowski, M. Secchi, M. Montagna, R. D. Priestley, E. M. Furst, and G. Fytas, Nat. Commun. **9**, 2918 (2018).
[17] W. Ogieglo, K. Tempelman, S. Napolitano, and N. E. Benes, J. Phys. Chem. Lett. **9**, 1195 (2018).
[18] L. Zhu, C. W. Brian, S. F. Swallen, P. T. Straus, M. D. Ediger, and L. Yu, Phys. Rev. Lett. **106**, 256103 (2011).
[19] W. Zhang and L. Yu, Macromolecules **49**, 731 (2016).
[20] I. Tanis, K. Karatasos, and T. Salez, J. Phys. Chem. B **123**, 8543 (2019).
[21] W. W. Mullins, J. Appl. Phys. **28**, 333 (1957).
[22] H. Le-The, C. Tregouet, M. Kappl, M. Müller, K. Kirchhoff, D. Lohse, A. van den Berg, M. Odijk, and J. C. T. Eijkel, Nanotechnology **30**, 065301 (2009).
[23] Y. Chai, T. Salez, and J. A. Forrest, Macromolecules **53**, 1084 (2020).
[24] P. De Gennes, Eur. Phys. J. E **2**, 201 (2000).
[25] S. T. Milner and J. E. Lipson, Macromolecules **43**, 9865 (2010).
[26] I. Siretanu, H. Saadaoui, J.-P. Chapel, and C. Drummond, Macromolecules **48**, 2787 (2015).
[27] F. Varnik, J. Baschnagel, and K. Binder, Phys. Rev. E **65**, 021507 (2002).
[28] J. Baschnagel and F. Varnik, J. Phys.: Condens. Matter **17**, R851 (2005).
[29] K. Ngai, A. Rizos, and D. Plazek, J. Non-Cryst. Solids **235**, 435 (1998).
[30] D. Long and F. Lequeux, Eur. Phys. J. E **4**, 371 (2001).
[31] J. E. G. Lipson and S. T. Milner, Eur. Phys. J. B **72**, 133 (2009).
[32] S. Mirigian and K. S. Schweizer, J. Chem. Phys. **141**, 161103 (2014).
[33] T. Salez, J. Salez, K. Dalnoki-Veress, E. Raphael, and J. A. Forrest, Proc. Natl. Acad. Sci. USA **112**, 8227 (2015).
[34] M. Arutkin, E. Raphaël, J. A. Forrest, and T. Salez, Soft Matter **13**, 141 (2016).
[35] Y. Wang and B. Bhushan, Soft Matter **6**, 29 (2010).
[36] D. Lohse and X. Zhang, Rev. Mod. Phys. **87**, 981 (2015).
[37] P. O'Connell and G. McKenna, Science **307**, 1760 (2005).

[38] Y. Wang, B. Zeng, X. Li, and X. Zhang, Adv. Mater. Interfaces **6**, 1900002 (2019).
[39] Y. Wang, X. Li, S. Ren, H. T. Alem, L. Yang, and D. Lohse, Soft Matter **13**, 5381 (2017).
[40] A. Silberberg, J. Colloid Int. Sci. **90**, 86 (1982).
[41] R. L. Jones, S. K. Kumar, D. L. Ho, R. M. Briber, and T. P. Russell, Nature **400**, 146 (1999).
[42] L. Si, M. V. Massa, K. Dalnoki-Veress, H. R. Brown, and R. A. L. Jones, Phys. Rev. Lett. **94**, 127801 (2005).
[43] O. Bäumchen, R. Fetzer, and K. Jacobs, Phys. Rev. Lett. **103**, 247801 (2009).
[44] C. K. Batchelor and G. Batchelor, *An Introduction to Fluid Dynamics* (Cambridge University Press, Cambridge, UK, 1967).
[45] R. Blossey, *Thin Liquid Films: Dewetting and Polymer Flow* (Springer Science & Business Media, Berlin, 2012).
[46] T. Salez, J. D. McGraw, O. Bäumchen, K. Dalnoki-Veress, and E. Raphaël, Phys. Fluids **24**, 102111 (2012).
[47] T. Salez, J. D. McGraw, S. L. Cormier, O. Bäumchen, K. Dalnoki-Veress, and E. Raphaël, Eur. Phys. J. E **35**, 114 (2012).
[48] S. Karpitschka, A. Pandey, L. A. Lubbers, J. H. Weijs, L. Botto, S. Das, B. Andreotti, and J. H. Snoeijer, Proc. Natl. Acad. Sci. USA **113**, 7403 (2016).
[49] M. Backholm, M. Benzaquen, T. Salez, E. Raphael, and K. Dalnoki-Veress, Soft Matter **10**, 2550 (2014).
[50] C. Pedersen, J. F. Niven, T. Salez, K. Dalnoki-Veress, and A. Carlson, Phys. Rev. Fluids **4**, 124003 (2019).
[51] A. Logg, K.-A. Mardal, and G. Wells, *Automated Solution of Differential Equations by the Finite Element Method: The FEniCS Book*, Vol. 84 (Springer Science & Business Media, Berlin, 2012).
[52] F. Chen, D. Peng, C.-H. Lam, and O. K. C. Tsui, Macromolecules **48**, 5034 (2015).
[53] H. Hasegawa, T. Ohta, K. Ito, and H. Yokoyama, Polymer **123**, 179 (2017).
[54] F. Brochard Wyart and P.-G. de Gennes, Eur. Phys. J. E **1**, 93 (2000).
[55] H. Bodiguel and C. Fretigny, Phys. Rev. Lett. **97**, 266105 (2006).
[56] K. Shin, S. Obukhov, J.-T. Chen, J. Huh, Y. Hwang, S. Mok, P. Dobriyal, P. Thiyagarajan, and T. Russell, Nat. Mater. **6**, 961 (2007).
[57] G. Reiter, Phys. Rev. Lett. **87**, 186101 (2001).
[58] P. Damman, N. Baudelet, and G. Reiter, Phys. Rev. Lett. **91**, 216101 (2003).
[59] J. Teisseire, A. Revaux, M. Foresti, and E. Barthel, Appl. Phys. Lett. **98**, 013106 (2011).
[60] P. Vettiger, G. Cross, M. Despont, U. Drechsler, U. Durig, B. Gotsmann, W. Haberle, M. A. Lantz, H. E. Rothuizen, R. Stutz, and G. K. Binnig, IEEE Trans. Nanotechnol. **1**, 39 (2002).